Road to fractals in a Yang-Mills system

Marcel Wellner

Department of Physics, Syracuse University, Syracuse, New York 13244-1130

A numerical profile is presented of the SU(2) Yang-Mills system in 2+1 dimensions. A particular set of smooth analytic initial conditions leads in a finite time to approximate fractalization of the potentials, fields, and energy density, plotted as functions of position. The system is chosen to be uniform in one of the spatial directions. The central result is a granulation (in one dimension) of the energy into a sprinkling of particlelike peaks with, so far, some background energy left over. The wave-number spectrum is found to spread very slowly in time. A simple algorithm is proposed for monitoring its progress.

PACS number(s): 05.45.+b, 11.15.−q

I. INTRODUCTION

Evidence for approximate fractals in a classical Yang-Mills system was published by this author some time ago [1]. The present article is a report on subsequent progress in this area, which addresses the evolution of fractals in space, starting from smooth analytic field configurations. More computing time has allowed the solutions to develop further; also, while Ref. [1] dealt exclusively with one potential, selected for its likely fractal nature, here we examine all three nontrivial potentials, as well as the fields and, most importantly, the gauge-invariant positive-definite energy density. The solution's spatial Fourier spectrum is analyzed as a function of time for clues as to the rate of approach to fractals. Throughout, we are dealing with a pure Yang-Mills system, i.e., one without Higgs, quark, or other extraneous fields.

Two considerations make the existence of Yang-Mills fractals plausible. First, a chaotic Yang-Mills regime (as a function of time) was announced in 1981 by Matinyan and collaborators [2–6]. The system originally chosen by these authors was the classical SU(2) field in 3+1 space-time dimensions, in the temporal gauge, with the couplings appropriate to that dimensionality, but without spatial dependence. The fields are then governed by ordinary differential equations rather than partial ones, and give rise to what was aptly named "Yang-Mills mechanics." Because the basic Lagrangian density is Lorentz invariant, it seems reasonable that a spatial counterpart to temporal chaos might exist if the uniformity conditions were relaxed.

A second hint of possible fractality is the lack of a preferred distance scale for the classical Yang-Mills field equations. (This is true regardless of the space-time dimensionality, in contrast to the quantized theory, where 3+1 dimensions are necessary for scale invariance.) It is only a hint because scale invariance, even where combined with nonlinearity, does not guarantee the appearance of fractals. As far as this author is aware, no spatial fractals have been reported in the context of other Lorentz invariant models. Indications of a developing spatial complexity have, however, been obtained by Furusawa [7] in the SU(2), 3+1 Yang-Mills system from initial potentials with a linear spatial dependence.

The notation will be as follows. In SU(n), let the potentials A^μ be a set of traceless Hermitian matrices, where $\mu = 0, 1, \ldots$ is the space-time index. The fields are

$$F^{\mu\nu} = \partial^\mu A^\nu - \partial^\nu A^\mu - ie[A^\mu, A^\nu] \tag{1}$$

for a coupling constant e, and the Lagrangian density is

$$\mathcal{L} = -\tfrac{1}{4}\mathrm{tr}(F^{\mu\nu}F_{\mu\nu}) . \tag{2}$$

The field equations are

$$D_\mu F^{\mu\nu} = 0 , \tag{3}$$

where

$$D_\mu = \partial_\mu - ie[A_\mu, \quad] \tag{4}$$

is the covariant derivative.

II. A CLASS OF REDUCED SOLUTIONS

Compared to a smooth solution, a fractal-like one puts far steeper demands on computing power; one reason lies in the huge number of lattice points required to reach even a moderate accuracy. Hence our first candidate for investigation should be a model that poses, computationally speaking, a (1+1)-dimensional problem. But a pure (1+1)-dimensional Yang-Mills system does not fill the bill, its solution being essentially trivial. (In the appropriate gauges it has a constant field in space-time.) Therefore we focus on a (2+1)-dimensional system made computationally 1+1 by requiring all potentials to depend on only one space dimension; this is enforced through the initial conditions. Because of an adequate number of components for potentials and fields, the system remains nontrivial.

From now on we assume the group SU(2), giving the potentials

$$A^\mu = \tfrac{1}{2}\sigma_a A_a^\mu \quad (\mu = 0, 1, 2, \quad a = 1, 2, 3) . \tag{5}$$

The σ_a are the Pauli matrices and the A_a^μ are nine real functions of space time.

Our initial conditions will always include

$$\partial_2 A^\mu = 0 \ , \quad \partial_0 \partial_2 A^\mu = 0 \quad (\mu = 0,1,2, \ x^0 = 0) \ . \tag{6}$$

The uniformity in x^2 is then propagated in time, so that the A^μ and $F^{\mu\nu}$ depend on x^0 and x^1 only.

We choose the temporal gauge

$$A_a^0 = 0 \quad (a = 1,2,3) \ , \tag{7}$$

which reduces the number of potentials to six. Furthermore, as indicated in Ref. [1], the system possesses a class of reduced solutions expressible in terms of three real potentials only,

$$A_3^2 = u \ , \quad A_1^1 = v \ , \quad A_2^2 = w \ , \tag{8}$$

with all other A_a^μ set equal to zero. This is a nontrivially self-consistent extension of the two-potential ansatz of Matinyan [5], and of an analogous two-potential ansatz that has found some use in the static case [8]. In what follows, all results are based on Eq. (8).

With the notation $x^0 = t$, $x^1 = x$, $x^2 = y$, the field equations, (3), now reduce to

$$(\partial_t^2 - \partial_x^2)u + e(2v\partial_x w + w\partial_x v) + e^2 v^2 u = 0 \ , \tag{9}$$

$$(\partial_t^2 - \partial_x^2)w - e(2v\partial_x u + u\partial_x v) + e^2 v^2 w = 0 \ , \tag{10}$$

$$\partial_t^2 v + e(u\partial_x w - w\partial_x u) + e^2(u^2 + w^2)v = 0 \ , \tag{11}$$

$$\partial_x \partial_t v + e(u\partial_t w - w\partial_t u) = 0 \ , \tag{12}$$

where Gauss's law, (12), results from $\nu = 0$ in (3). We note that the three equations (9), (10), and (11) are sufficient to propagate u, v, w from Cauchy initial data, and that therefore (12) is a constraint. The latter must be enforced by hand on the initial conditions, but maintains itself automatically thereafter, as can be verified from the time derivative of (12), with use of the remaining field equations.

III. SPACE-TIME SCALING AND INITIAL CONDITIONS

In terms of some constant ξ, the field equations (9)–(12) are invariant under the substitutions

$$u = \xi U \ , \quad u = \xi V \ , \quad w = \xi W \ , \tag{13}$$

$$t = T/\xi \ , \quad x = X/\xi \ , \tag{14}$$

with a fixed coupling constant e. Therefore the model has no preferred scale in space-time.

Alternatively, we can replace the amplitude scaling by a scaling of e,

$$e = \xi \bar{e} \quad \text{[instead of (13)]} \ . \tag{15}$$

Another alternative is to scale the amplitudes as well as the coupling constant; in this way we can, without loss of generality, standardize the field equations to unit coupling, $e \to 1$. In this paper, however, we prefer to regard e as adjustable.

We observe that, while the model is scale invariant, the initial conditions, and therefore the solutions, in general are not. In particular, consider two families of initial conditions which break the scale invariance of x and also

allow a simple enforcement of Gauss's law (12). With real parameters a, b, we have type I (u,v,w symmetric in time):

$$u = a \ , \quad \partial_t u = 0 \ ,$$

$$v = 0 \ , \quad \partial_t v = 0 \ , \tag{16}$$

$$w = b \sin x \ , \quad \partial_t w = 0 \ ,$$

and type II (u symmetric in time; v, w antisymmetric in time):

$$u = a \ , \quad \partial_t u = 0 \ ,$$

$$v = 0 \ , \quad \partial_t v = abe \cos x \ , \tag{17}$$

$$w = 0 \ , \quad \partial_t w = b \sin x \ .$$

In the above we have taken, without loss of generality, a wavelength 2π for the spatial nonuniformity.

Thus, for a fixed coupling, the initial conditions break the scale invariance through the wavelength of the initial modes and/or through the chosen amplitudes of these modes. Why then should we expect the existence of fractals? The answer is that the system will forget its initial conditions, at least locally, if its behavior becomes sufficiently stochastic. We shall present what indications we have that such a scenario really takes place.

Globally some memory must remain, because total energy and momentum are conserved; some spatial periodicity and parity properties must persist as well. In addition to the periodicity under $x \to x + 2\pi$, we have the following, valid for both types I and II solutions at all times:

$$u(x) = u(-x) \ , \quad v(x) = v(-x) \ , \quad w(x) = -w(-x) \ ,$$

$$u(x) = u(\pi - x) \ , \quad v(x) = -v(\pi - x) \ , \tag{18}$$

$$w(x) = w(\pi - x) \ .$$

Since these reflection symmetries are about $x = 0$ and $x = \pi/2$, we only need to calculate solutions within the interval $0 \le x \le \pi/2$. Furthermore, Eqs. (18) imply

$$v(\pi/2) = w(0) = 0 \ ,$$

$$\partial_x u(0) = \partial_x u(\pi/2) = \partial_x v(0) = \partial_x w(\pi/2) = 0 \tag{19}$$

at all times.

IV. FIELDS, ENERGY, AND MOMENTUM

The fields

$$E_x = F^{10} \ , \quad E_y = F^{20} \ , \quad B = -F^{12} \tag{20}$$

amount in the temporal-gauge reduced solution to only five nonzero SU(2) components,

$$E_{x1} = -\partial_t v \ , \quad E_{y2} = -\partial_t w \ , \quad E_{y3} = -\partial_t u \ ,$$

$$B_2 = \partial_x w + euv \ , \quad B_3 = \partial_x u - evw \ , \tag{21}$$

with symmetries corresponding to (18), namely,

$$E_{x1}(x)=E_{x1}(-x) \ , \quad E_{y2}(x)=-E_{y2}(-x) \ ,$$

$$E_{y3}(x)=E_{y3}(-x) \ ,$$

$$B_2(x)=B_2(-x) \ , \quad B_3(x)=-B_3(-x) \ ,$$

$$E_{x1}(x)=-E_{x1}(\pi-x) \ , \quad E_{y2}(x)=E_{y2}(\pi-x) \ ,$$

$$E_{y3}(x)=E_{y3}(\pi-x) \ ,$$

$$B_2(x)=-B_2(\pi-x) \ , \quad B_3(x)=-B_3(\pi-x) \ ,$$

(22)

valid at all times.

Using the gauge-invariant energy-momentum tensor

$$T^{\mu\nu}=-F_a^{\mu\lambda}F_{\lambda a}^{\nu}+\tfrac{1}{4}g^{\mu\nu}F_a^{\kappa\lambda}F_{\kappa\lambda a} \ , \tag{23}$$

we have the energy density

$$T^{00}=\tfrac{1}{2}[(E_{x1})^2+(E_{y2})^2+(E_{y3})^2+(B_2)^2+(B_3)^2] \tag{24}$$

and the two components of momentum density,

$$T^{10}=E_{y2}B_2+E_{y3}B_3 \ ,$$

$$T^{20}\equiv 0 \ . \tag{25}$$

The total energy in the interval $0<x<\pi/2$, and per unit y interval, obeys the continuity equation

$$\frac{d}{dt}\int_0^{\pi/2}T^{00}dx=-T^{01}\Big|_0^{\pi/2}=0 \ . \tag{26}$$

The vanishing is due to (22) taken at 0 and $\pi/2$.

The following alternative expression is obtained with the help of the field equations:

$$T^{00}=\tfrac{1}{2}[(\partial_t v)^2+(\partial_t u)^2-u\partial_t^2 u+(\partial_t w)^2$$
$$-w\partial_t^2 w+\partial_x(u\partial_x u+w\partial_x w)] \ , \tag{27}$$

leading to the computationally useful

$$\mathcal{E}=\int_0^{\pi/2}T^{00}dx$$
$$=\tfrac{1}{2}\int_0^{\pi/2}[(\partial_t v)^2+(\partial_t u)^2-u\partial_t^2 u$$
$$+(\partial_t w)^2-w\partial_t^2 w]dx \ . \tag{28}$$

[The boundary terms vanish by (19)].

The initial fields and energy are, for type I solutions,

$$E_{x1}=E_{y2}=E_{y3}=0 \ ,$$

$$B_2=b\cos x \ , \quad B_3=0 \ ,$$

$$\mathcal{E}=\pi b^2/8 \ . \tag{29}$$

For type II solutions

$$E_{x1}=-abe\cos x \ , \quad E_{y2}=-b\sin x \ , \quad E_{y3}=0 \ ,$$

$$B_2=B_3=0 \ ,$$

$$\mathcal{E}=(\pi b^2/8)(a^2e^2+1) \ . \tag{30}$$

Turning to the momentum, we note that it is *not* conserved in the interval $(0,\pi/2)$, owing to transfers across the end points. However, over $(0,\pi)$, we have

$$\int_0^{\pi}T^{10}dx=\int_0^{\pi}(E_{y2}B_2+E_{y3}B_3)dx=0 \ . \tag{31}$$

It can be verified that the transfers across 0 and π cancel. In short, the total x momentum vanishes in $0\leq x\leq\pi$, and the y-momentum density vanishes identically; both momentum components are trivially conserved.

The remainder of this study is devoted to a single set of initial conditions, namely, type II, Eq. (17), with

$$a=b=1 \ , \quad e=64 \ . \tag{32}$$

These numbers are not the result of a search; the large e is a first reasonable trial, leading also to a large $\partial_t v$ in (17); the behavior that emerges therefore seems to be in some sense typical of the systems's nonlinearity.

While an exploration of the initial parameter space would be of interest, the substantial amount of computing has so far made it advisable to concentrate on one solution; but even in this restricted context, larger values of the time variable may well bring to light new aspects of the system.

V. REPRESENTATIVE PLOTS

The numerical plots have been recorded over the spatial interval $(0,\pi/2)$. On the same scale $(c=1)$, time has been allowed to run over $0\leq t\leq 8$. As discussed further on, the computer's processing time rises ever faster with increasing t and thus imposes on it a rather strict, if provisional, upper bound.
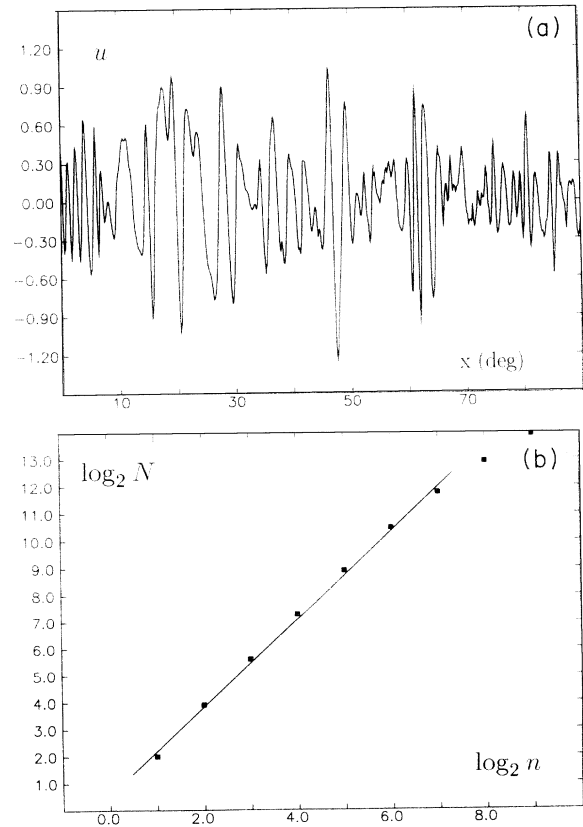

FIG. 1. (a) The potential $u(x)$ at $t=8$. The appearance of $w(x)$ (not shown) is quite similar. (b) Box-dimension plot for (a). The dimension is $D(u)=1.65$.

Figures 1–4 display in parts (a) the results at $t=8$; a light signal sent at $t=0$ could have crossed the width of the frame about five times. The functions illustrated are the potentials u, v, and the field components E_{x1}, E_{y3}. The x axis is labeled in degrees.

The early results [1] indicated a smooth time dependence of the potentials. This is no longer the case for $6 < t < 8$, at least when compared with the spatial behavior on the same scale. Figures 5 and 6 illustrate that observation at $x=45°$.

In searching for a more fundamental characterization of the system's behavior we examine the positive-definite, gauge-invariant energy density T^{00}, Eq. (24), and thus obtain what is perhaps the central result of this work. At times $t=6$ and 8 we find the plots shown in Figs. 7 and 8(a). The initially smooth and analytic distribution has turned into almost a sprinkling of particles. The change that occurs between $t=6$ and 8 demonstrates that bulk transfers of energy are present as well.

VI. TOWARDS SELF-AFFINE FRACTALS

The most obvious feature of the present results is the generation of an irregular spatial dependence, starting from the smooth analytic conditions described above; the degree of irregularity, which appears to increase with time, is amenable to fractal analysis.

What kind of fractal should we be looking for? A self-similar fractal set yields subsets that can be isotropically magnified by a scale factor ξ so as to be indistinguishable from the original whole set; the self-similarity can be exact or statistical.

The sets of interest to us here are single-valued functions $f(x)$, plotted in a two-dimensional space f versus x. Such sets, for example in the theory of noise, have been well studied in terms of their fractal properties, and are known to be generally self-affine rather than self-similar [9]. This means that a subset can be isolated (in practice the portion of curve enclosed between two chosen values of x), and magnified by different scale factors ξ and ϕ in the x and f directions, such that the magnified segment is then statistically indistinguishable from the whole curve.

An actual plotted curve, or one obtained by a continuous deformation from a smooth shape, cannot be a true fractal. The reason is that successive magnifications eventually reveal details of the set which are themselves smooth, or perhaps consist of detached points, and thus no longer resemble the original curve. We can, however, speak of approximate fractals. Here self-affinity means that we consider a plot P, from which we select a piece Q. We then magnify Q anisotropically by appropriate scale factors, thus obtaining a plot Q', which necessarily contains less information than P. However, Q' should be statistically indistinguishable from a lower-resolution replot-
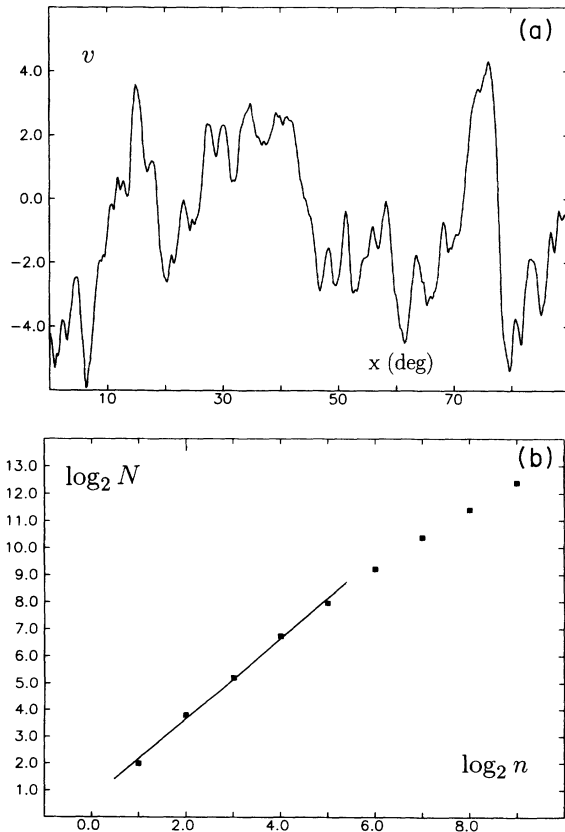

FIG. 2. (a) The potential $v(x)$ at $t=8$. (b) Box-dimension plot for (a). We find $D(v)=1.5$.
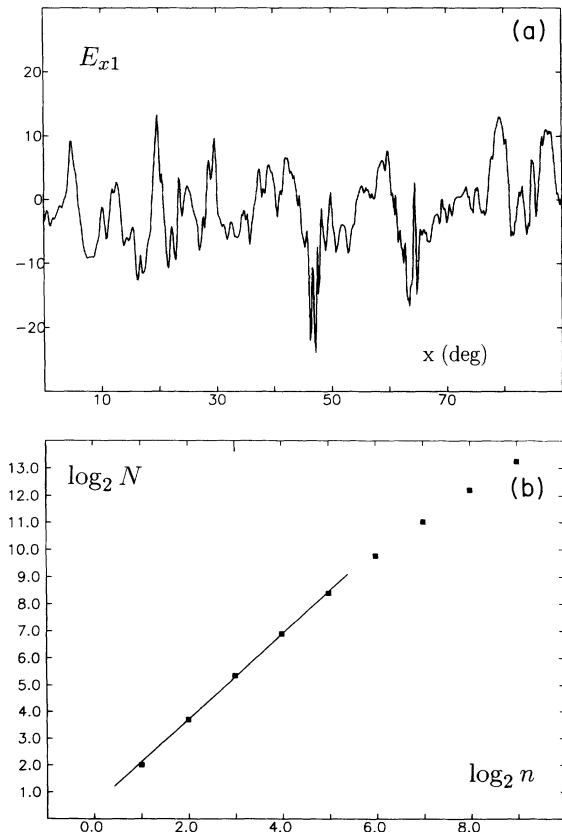
FIG. 3. (a) The field $E_{x1}(x)$ at $t=8$. (b) Box-dimension plot for (a). We find $D(E_{x1})=1.6$.
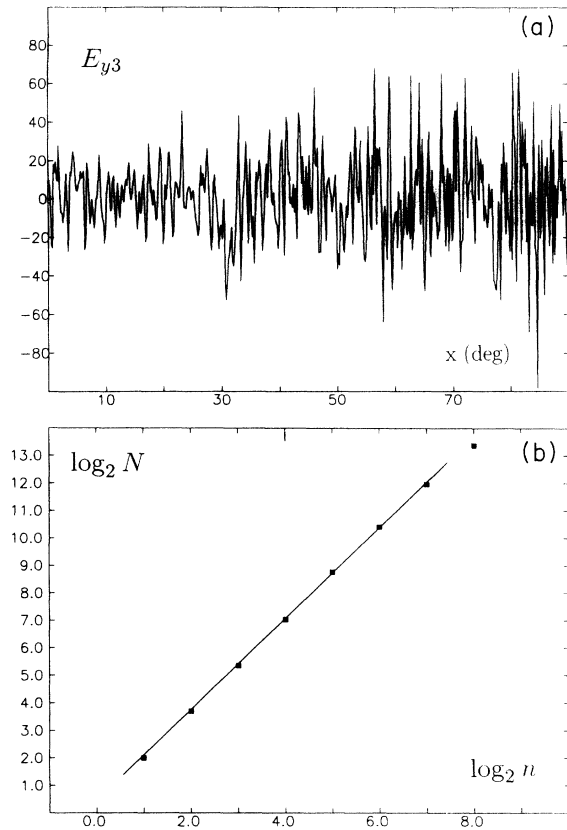
FIG. 4. (a) The field $E_{y3}(x)$ at $t=8$; the fields E_{y2}, B_2, B_3 (not shown) have a similar appearance. (b) Box-dimension plot for (a). We find $D(E_{y3})=1.66$.

ting, R, of P. Starting with Fig. 4(a), this process is demonstrated qualitatively in Figs. 9(a) and 9(b).

The fractal dimension of the above-mentioned plots has been determined by the box-counting method, in which each axis of the frame is subdivided into n equal intervals. Of the resulting n^2 boxes, a number N are occupied by portions of the curve. The box-counting dimension is then defined as

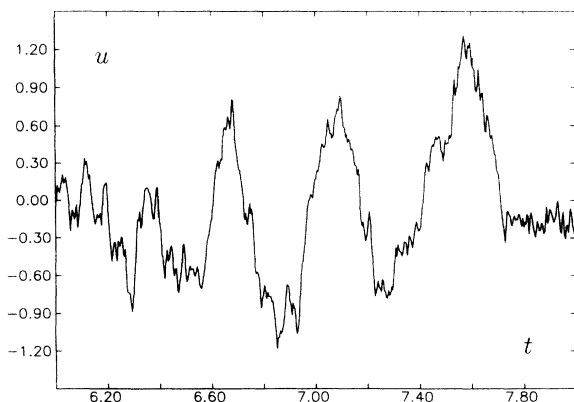$$D = \lim_{n \to \infty} \frac{\log_b N}{\log_b n} \tag{33}$$

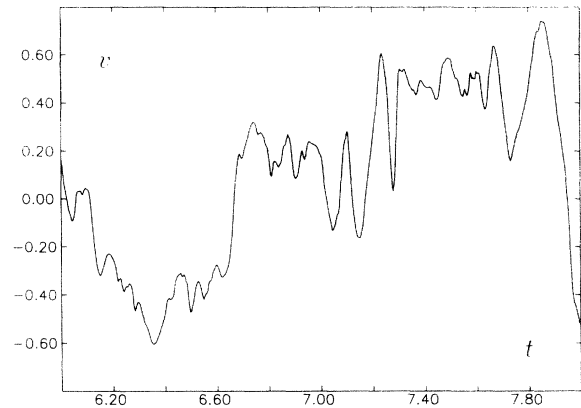FIG. 5. The potential $u(t)$ at $x=45°$. A similar appearance is found for $w(t)$ (not shown).

FIG. 6. The potential $v(t)$ at $x=45°$.

for any base b.

Nontrivial curves will have $D > 1$. In practice, however, the limit $n \to \infty$ cannot be taken; at sufficiently large n the grid begins to detect the smooth curve and the limit reaches 1, or even zero if the plot consists of individual points. The usual method for empirical fractals is to plot $\log_b N$ against $\log_b n$, and to discard the values of n above the onset of unit slope. To the extent that the remaining plot is linear, it characterizes a fractal, and its slope is the box-counting dimension. In the present work, n is taken to be a power of 2, leading to fractal-dimension plots for $\log_2 N$ against $\log_2 n$. The initial box ($n=1$) is chosen as the minimal one that will contain the whole range of the curve in the domain $0 \le x \le \pi/2$. Each log-log plot is shown next to the approximate fractal from which it is obtained. The approximate dimensions are listed in Table I.

The general conclusions are as follows.

(1) Except for the potential v, we consider six or seven log-log points to be well enough aligned, indicating incipient fractal behavior. For v we have fewer points (four or five), to the extent that its fractal behavior must be considered less certain.

(2) Although the complexity of the solutions increases substantially with time, the number of relevant points in the log-log plots hardly increases at all in the time range exhibited. This phenomenon is presumably related to the extremely slow spreading of the solution's spectrum in wave-number space as discussed in Sec. VII.

(3) The estimated fractal dimension shows little change

TABLE I. Box-counting dimensions D. The results are based on a scale range of 2^n.

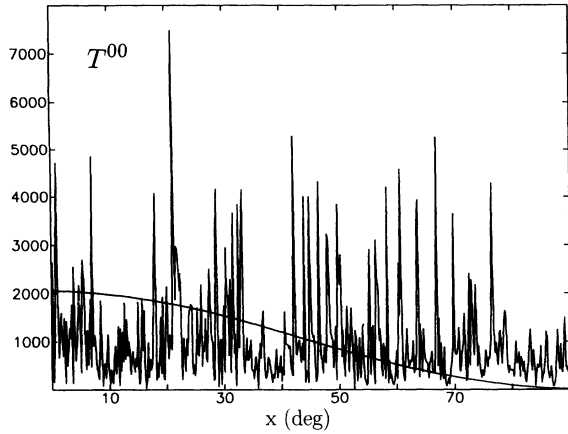| Function	$t=6$		$t=8$	
	D	n	D	n
u	1.62	6	1.65	7
v	1.5	5	1.5	5
w	1.63	6	1.64	7
E_{x1}	1.5	5	1.6	5
E_{y2}	1.70	7	1.69	7
E_{y3}	1.73	7	1.66	7
B_2	1.69	7	1.74	7
B_3	1.74	7	1.72	7
T^{00}	1.68	7	1.69	8

FIG. 7. The positive-definite gauge-invariant energy density $T^{00}(x)$ at $t=6$, compared with its plot at $t=0$ (smooth curve).

over time.

(4) At $t=8$, the following pairs of functions are characterized by rather close fractal dimensions: u and w; E_{y2} and E_{y3}; B_2 and B_3. On the other hand, v has a substantially smaller dimension than the other two potentials, and E_{x1}, which derives from v, has a smaller dimension than the other fields; refer to Eqs. (21). The fields tend to have somewhat larger dimensions than the potentials.

(5) The best fractal candidate turns out to be the energy density. It provides us with seven or eight well-
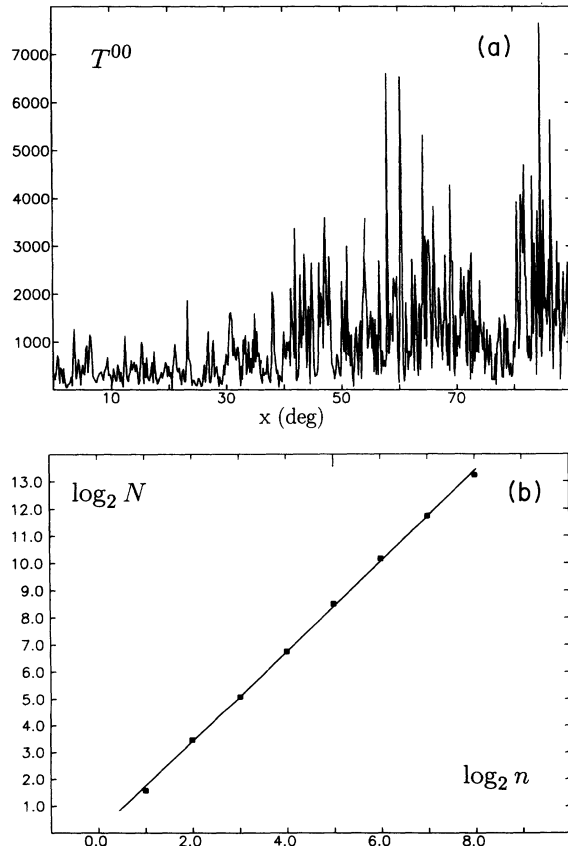

FIG. 8. (a) The energy density $T^{00}(x)$ at $t=8$. (b) Box-dimension plot for (a). We find $D(T^{00})=1.69$.
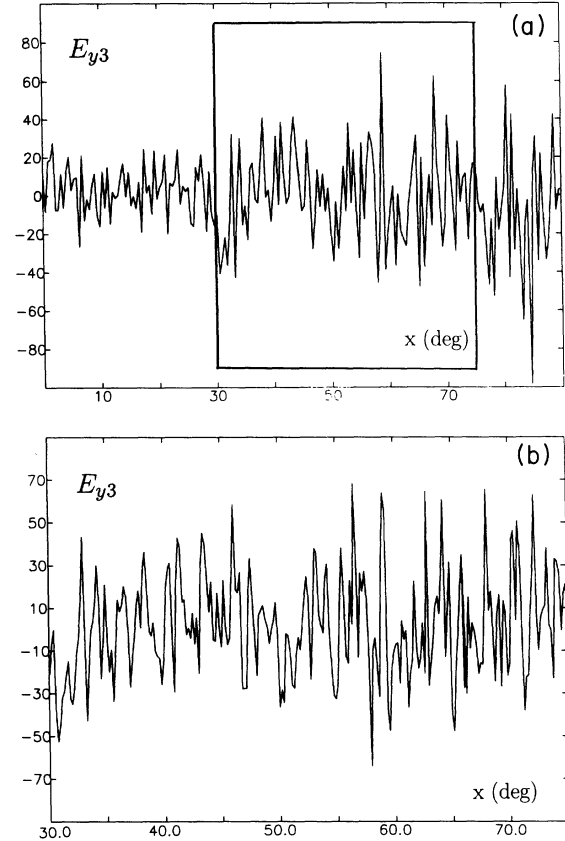

FIG. 9. (a) A lower-resolution replotting of Fig. 4(a); the framed subset is to be scaled up. (b) The scaled-up subset of (a); the resolution, however, is the original one of Fig. 4(a).

aligned log-log points, showing a box-counting dimension of 1.69.

VII. SPREADING OF THE MODES

The spatial spectra of the potentials are defined by

$$u(x,t)=\sum_{k=0}^{\infty} u_k(t)\cos kx ,$$

$$v(x,t)=\sum_{l=1}^{\infty} v_l(t)\cos lx , \qquad (34)$$

$$w(x,t)=\sum_{m=1}^{\infty} w_m(t)\sin mx ,$$

where the symmetries imply that the only nontrivial modes are for k even, l odd, and m odd. The initial spectra, including time derivatives, consist of two modes only: $k=0$, and $l=m=1$. Their appearance at $t=8$ is shown in Figs. 10(a) and 10(b).

The spreading in wave-number space is of interest for a number of reasons.

(1) Historically, the best-known study of wave-number spreading in a field theory is that of Fermi, Pasta, and Ulam [10]. Their model, a discrete chain of nonlinearly coupled oscillators, unexpectedly showed negligible spreading of modes and near recurrences to initial conditions. Such phenomena are not seen in the present work.
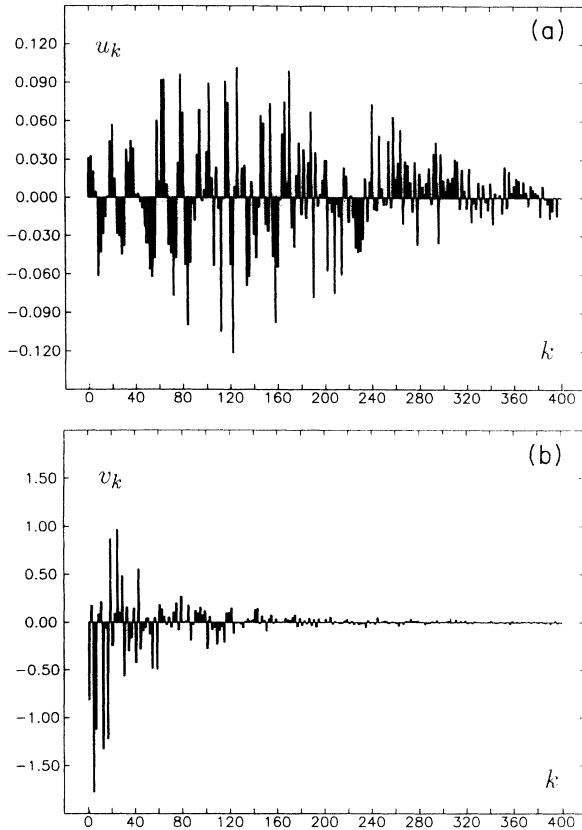
FIG. 10. (a) The main portion of the wave-number spectrum for u at $t = 8$. The computational cutoff is at $k = 1440$. (b) The spectrum of v at $t = 8$.

FIG. 11. The mode fronts for u (left points of doublets) and w (right points) as functions of time. The amplitudes are chosen to be a factor 10 apart. The steplike line indicates the calculational cutoff.

(2) The shape of the wave-number spectrum might be expected to approach (statistically) a power law, as found in the frequency spectra of noise. In the present case, however, the large wave-number tail of the spectrum gradually advances as additional modes are excited, and thus this part of the spectrum is badly distorted compared to its hypothetical ultimate appearance. As a consequence, no simple interpretation can yet be offered here for the overall spectral shape.

(3) We are solving a set of coupled ordinary differential equations for the amplitudes u_k, v_l, w_m as functions of time. The computational wave-number cutoff K_{max} should be larger than the natural cutoff of the spectral tail. Since the latter is advancing with time, we must either take a fixed K_{max} large enough to accommodate the whole spectrum up to the largest value of t, or, more economically, an advancing K_{max} that maintains a safe distance from the spectral tail. The latter course has been taken, and requires monitoring of the spectrum.

(4) A fractal curve has an infinite amount of small-scale structure, and hence its spectrum extends to infinite wave numbers. Correspondingly, in the box-counting procedure, information is gathered from arbitrarily small boxes, and the approach of the actual curves to fractal shapes is reflected in the increasing number of aligned points in the dimensional log-log plots. Therefore the number of good points is related to the high end of the spectrum. A heuristic way to estimate one from the oth-
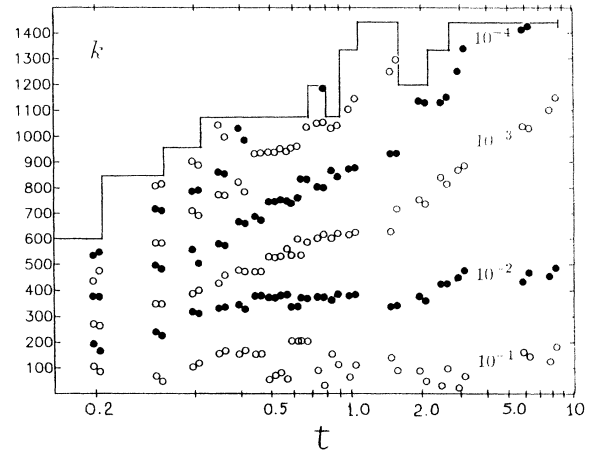
er is presented below.

Figure 11 gives an overview of the spectral development after $t = 0.15$, a time which marks the beginning of the spectrum's slow-spreading regime. The points in that plot represent the location in wave-number space of spreading sections of the spectral tail. Just as a wave in space can have identifiable wave fronts whose motion characterizes its propagation, its spectrum in wave-number space can be considered, at least in its tail end, to have "mode fronts" that characterize the rate of spreading in that space. The mode fronts are conveniently tagged by their amplitude; the following method is simple and well adapted to an irregular spectrum whose outer edge one wishes to track.

Consider for definiteness the spectrum u_k $(k = 0, 1, 2, \ldots)$. To select a mode front, we choose a numerical amplitude $U > 0$, and define the location K of the mode front as being the largest value of k such that $u_k \geq U$. In other words, we have $K = K(U)$ such that

$$u_k < U \quad (\text{all } k > K) , \quad u_K \geq U . \tag{35}$$

The progress of K as a function of time indicates the rate of spreading of the spectrum. Two remarks are in order at this stage.

(a) It is found that the low wave-number portions of the spectra for u and w do not change their typical amplitudes, which remain of order 0.1 during all observed times. Thus the spectral shift towards larger wave numbers does not have an overall rise or fall of the amplitudes as a contributing cause.

(b) The moments of the "power spectra" u_k^2, etc., which might be expected to indicate their extent in wave-number space, are in fact unreliable clues to the spread of their extreme tails. For example, the mean square wave number is found to rise and fall in a manner unrelated to that spread.

Figure 11 plots the wave-number location of the mode fronts for u and w. The points are alternately hollow and solid in order to keep the mode fronts apart visually. The fronts' amplitudes are 10^{-1}, 10^{-2}, $10^{-3}, \ldots$ as labeled.
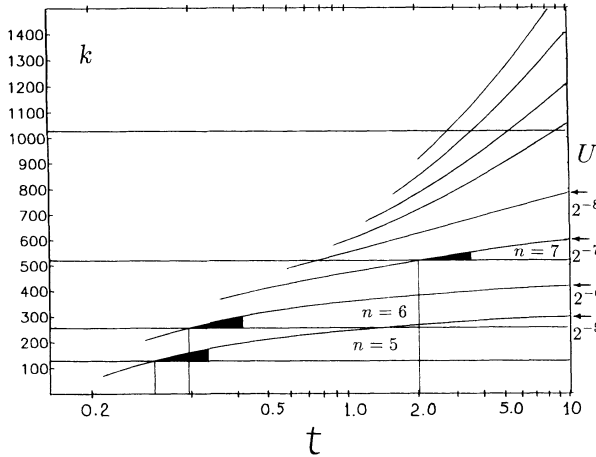
FIG. 12. A schematic version of Fig. 11 with amplitudes a factor 2 apart. The number of good points on the box-dimension plots for u is denoted by n. To obtain that many good points, the corresponding shaded edge is expected to give a lower bound on t.

Each doublet has one point for u (left) and one for w (right), slightly offset to the left and right of their actual common time coordinate. The time scale is logarithmic in $t - 0.15$, attesting to the exceedingly slow progress of the mode fronts. The steplike solid line represents the computational cutoff; see the Appendix.

In addition to helping with managing the cutoff, the mode-front plot is useful in assessing the expectation for additional aligned points in the dimensional log-log plots. A plausibility argument can be made on the basis of Fig. 12, an idealization of Fig. 11 with factors of 2, rather than 10, between the amplitude steps.

We consider one high mode, say with amplitude u_k, and ask under what conditions it contributes significantly to the nth point in the log-log plot. We assume for the sake of discussion that mode k is an isolated one, in the sense that it is visible as a ripple on an otherwise smoother function $u(x)$. There are 2^n divisions along the x axis, and the mode, when sampled by that many horizontal bins, should no longer appear smooth. Conversely, in order to see the horizontal bin structure, the mode should have a maximum wavelength $2\pi/k \approx (\pi/2)/2^n$, which gives

$$k \gtrsim 2^{n+2} . \tag{36}$$

Next, the amplitude $|u_k|$ itself must exceed the height of about one box in order to be recognized as a ripple. Since the complete frame has approximately unit height, we need

$$|u_k| \gtrsim 2^{-n} . \tag{37}$$

Thus, according to (36) and (37), the modes contributing to the nth log-log point are located, on Fig. 12, above the horizontal line $k = 2^{n+2}$ and below the amplitude locus $U = 2^{-n}$. These regions (with shaded tip) begin at points A, B, C. The minimum times rise steeply with n. They are 0.27 for $n = 5$, 0.30 for $n = 6$, 2.0 for $n = 7$, and extrapolate to far beyond 10 for $n = 8$ and higher. Those re-

sults point to the need for substantially more computing time or power if additional points are to be sought on the dimensional log-log plots; see also the Appendix.

VIII. SUMMARY AND DISCUSSION

Within the present model, and based on considerably more data than Ref. [1], we have demonstrated the evolution of spatial structure on an increasingly fine scale, starting from a smooth analytic field configuration; it is likely that the process continues indefinitely. The approximately fractal nature of the space dependence is documented for two of the three nontrivial potentials (u and w), and the data are at least consistent with a fractal evolution for the third potential (v) as well. Spatial scaling extends at best over a factor of 2^6 or 2^7 for the potentials and fields, while for the energy density the factor is 2^7 or 2^8. An improvement in these figures would require more extensive computing. We note that the longest time of evolution investigated here is 8.0, compared to a spatial extent of $\pi/2$. We see therefore that longer times are needed before a permanent trend can be reliably forecast. We note, also, the exceedingly slow spreading of the spectrum in wave-number space, a circumstance related to the slow acquisition of good points in the dimensional log-log plots.

Our main result is a granulation (in one dimension) into what appears to be a sprinkling of many particles of assorted energies, with some background energy density left over. Toy models of galaxy distribution [11] might well be attempted on this basis, as was already remarked in Ref. [1] on more tentative grounds.

The formation of fractals is related to the fact that the solution forgets its initial conditions except for some global conservation laws (energy, momentum, and spatial symmetries including periodicity). The strongest confirmation of this phenomenon is found in the emerging statistical indistinguishability between the potentials u and w. The one-parameter global gauge transformation

$$A^\mu \to U A^\mu U^{-1} ,$$
$$U = \exp(i\chi\sigma_1/2) \tag{38}$$

induces the rotation

$$u \to u \cos\chi + w \sin\chi ,$$
$$w \to -u \sin\chi + w \cos\chi , \tag{39}$$
$$v \to v ,$$

under which the set of reduced solutions (8) is mapped into itself. Since the field equations (9)–(12) are invariant under (39), any distinction between u and w must arise from their (very different) initial conditions. But at sufficiently late times ($t \gtrsim 6$) we can hardly distinguish statistically between their plots, or between other plots that are similarly gauge related [see conclusion (4) of Sec. VI]; initial conditions have been forgotten.

It is interesting that the solution also "tries to forget" initial conditions that are actually unforgettable, namely, the boundary conditions (19) at $x = 0$, $\pi/2$. These conditions are no longer visible in the above-mentioned figures

except under magnification. The situation is somewhat reminiscent of a Fourier expansion under inappropriate boundary conditions—a feasible procedure of which the price is the Gibbs phenomenon. There is so far no evidence for anything like a Gibbs phenomenon in our case, however.

A fractal Yang-Mills behavior may have implications in the path-integral formulation of particle theory. The integrand contains the factor $\exp(iS/\hbar)$, where S is the classical action. In evaluating S, solutions as well as non-solutions of the classical field equations must be considered; but in a steepest-descent evaluation, the solutions are generally expected to dominate the path integral. If the fractal solutions have to be included, the usually moderate number of lattice points seem inadequate. Therefore the validation of lattice results needs to include an argument to the effect that the fractal cases are of negligible weight. Alternatively, it would have to be demonstrated that the presence of a mass input, which selects a scale, prevents the development of fractals in the limit of much finer scales. Similar concerns have already been expressed [12] in relation to chaotic behavior. (It must be noted that path-integral calculations are apt to be done in the Euclidean version of the theory. One might hope that fractal-related difficulties would thereby be avoided, but, again, this would need to be demonstrated.)

ACKNOWLEDGMENTS

APPENDIX: COMPUTATIONAL REMARKS

The field equations have been solved in terms of the amplitudes u_k, v_l, w_m in (34). Cutting off the spectrum, at the latest times, to 720 nontrivial modes, we have a set of $(3)(720) = 2160$ coupled ordinary differential equations. The calculations were done in 64 bit precision on a Cray YMP C90 machine. The accuracy was checked as follows.

Up to $t = 0.4$, the propagation was driven by Eqs. (9)–(11); Gauss's law, Eq. (12), was used for quality control. This represents a set of as many conditions as we have modes, and tests the overall consistency, as well as the code and its accuracy. Starting from

$$\partial_x \partial_t v = -e(u \partial_t w - w \partial_t u) ,\qquad\qquad \text{(A1)}$$

TABLE II. Lattice density and conservation of energy. d is lattice density in points/unit time; δ is fractional deviation from initial energy, measured at end of run.

t	d	δ
0–0.05	10^5	1.6×10^{-7}
0.05–3.00	10^5	3.9×10^{-6}
3.00–6.00	5×10^4	1.1×10^{-4}
6.00–8.00	7.5×10^4	1.2×10^{-4}

and Fourier analyzing both sides, we have the generic form

$$L(k,t) = R(k,t) \quad (k = 0, 2, 4, \ldots, k_{\max}) . \qquad \text{(A2)}$$

Its breakdown was measured by $(L-R)/(|L|+|R|)$. For $k = 0$ this number was kept below 10^{-7} through $t = 0.4$. With 540 nontrivial modes a 1% breakdown was reached at the 388th nontrivial mode; here the amplitudes are already a factor of 10^{-5} below their values at small k. The lattice density for integration was 10^5 points/(unit time).

Over long times, Gauss's law necessarily deteriorates owing to the residual numerical errors. Accordingly, the present results were obtained with an enforcement of Gauss's law at every step, as a substitute for the $\partial_t^2 v$ equation (11). The loss of Gauss's law as a diagnostic was partly made up by repeating all previous calculations, with unchanged results, and by monitoring the conservation of total energy.

Two approximation parameters must be considered: the wave-number cutoff $k_{\max}$, and the lattice density d in the time direction. The jagged appearance of the cutoff in Fig. 11 reflects in small part considerable experimentation with $k_{\max}$: the spectrum, including its tail almost up to the cutoff, is insensitive to it. The conservation of energy, as well, is independent of $k_{\max}$ in the range considered. The computer's CPU time increases approximately as $(k_{\max})^2$.

On the other hand, the conservation of energy is quite sensitive to the lattice density, at least up to the highest densities used. Conservation becomes consistently better with larger d, demonstrating the stability of the algorithm. Let the fractional energy nonconservation be

$$\delta = (\mathcal{E} - \mathcal{E}_0)/\mathcal{E}_0 , \qquad\qquad \text{(A3)}$$

where $\mathcal{E}$ is the energy computed at any time from Eq. (28), and $\mathcal{E}_0$ is the initial energy, $\mathcal{E}_0 = 1608.8881$ from Eq. (30). Table II shows the value of d in successive time intervals, with δ at the end of each interval. The CPU time increases approximately linearly with d.

[1] M. Wellner, Phys. Rev. Lett. **68**, 1811 (1992).
[2] S. G. Matinyan, G. K. Savvidi, and N. G. Ter-Arutyunyan-Savvidi, Zh. Eksp. Teor. Fiz. **80**, 830 (1981) [Sov. Phys. JETP **53**, 421 (1981)].
[3] B. V. Chirikov and D. L. Shepelyanskiĭ, Pis'ma Zh. Eksp. Teor. Fiz. **34**, 171 (1981) [JETP Lett. **34**, 163 (1981)].
[4] S. G. Matinyan, G. K. Savvidi, and N. G. Ter-Arutyunyan-Savvidi, Pis'ma Zh. Eksp. Teor. Fiz. **34**, 613 (1981) [JETP Lett. **34**, 590 (1981)].
[5] A review paper: S. G. Matinyan, Fiz. Elem. Chastits. At. Yadra **16**, 522 (1985) [Sov. J. Part. Nucl. **16**, 226 (1985)].
[6] S. G. Matinyan, E. P. Prokhorenko, and G. K. Savvidi, Pis'ma Zh. Eksp. Teor. Fiz. **44**, 109 (1986) [JETP Lett. **44**, 138 (1986)].

[7] T. Furusawa, Nucl. Phys. **B290**, [FS20], 469 (1987).

[8] M. Wellner, Phys. Rev. D **41**, 1255 (1990).

[9] B. B. Mandelbrot, Phys. Scr. **32**, 257 (1985); and in *Fractals in Physics,* edited by L. Pietronero and E. Tosatti (Elsevier, Amsterdam, 1986); R. F. Voss, in *Scaling Phenomena in Disordered Systems,* edited by R. Pynn and A. Skjeltorp (Plenum, New York, 1985). See also *Dynamics of Fractal Surfaces,* edited by F. Family and T. Vicsek (World Scientific, Singapore, 1991).

[10] E. Fermi, J. Pasta, and S. Ulam, Los Alamos Scientific Report No. LA-1940, 1955 (unpublished); E. Fermi, *Collected Papers* (University of Chicago Press, Chicago, 1965), Vol. II, p. 978; see also R. Z. Sagdeev, D. A. Usikov, and G. M. Zaslavsky, *Nonlinear Physics* (Harwood, Chur, Switzerland, 1988); M. Toda *et al., Statistical Physics I,* 2nd ed. (Springer, New York, 1991).

[11] For a fractal interpretation of the existing data, see P. H. Coleman and L. Pietronero, Phys. Rep. **213**, 313 (1992).

[12] M. C. Gutzwiller, *Chaos in Classical and Quantum Mechanics* (Springer, New York, 1990), p. 98; B. Müller and A. Trayanov, Phys. Rev. Lett. **68**, 3387 (1992).